

Neuronal Excitability

Cerebellar Stellate Cell Excitability Is Coordinated by Shifts in the Gating Behavior of Voltage-Gated Na⁺ and A-Type K⁺ Channels

Ryan P.D. Alexander,^{1,2} John Mitry,³ Vasu Sareen,³ Anmar Khadra,³ and  Derek Bowie²

<https://doi.org/10.1523/ENEURO.0126-19.2019>

¹Integrated Program in Neuroscience, McGill University, Montréal, Quebec H3A 2B4, Canada, ²Department of Pharmacology and Therapeutics, McGill University, Montréal, Quebec H3G 1Y6, Canada, and ³Department of Physiology, McGill University, Montréal, Quebec H3G 1Y6, Canada

Abstract

Neuronal excitability in the vertebrate brain is governed by the coordinated activity of both ligand- and voltage-gated ion channels. In the cerebellum, spontaneous action potential (AP) firing of inhibitory stellate cells (SCs) is variable, typically operating within the 5- to 30-Hz frequency range. AP frequency is shaped by the activity of somatodendritic A-type K⁺ channels and the inhibitory effect of GABAergic transmission. An added complication, however, is that whole-cell recording from SCs induces a time-dependent and sustained increase in membrane excitability making it difficult to define the full range of firing rates. Here, we show that whole-cell recording in cerebellar SCs of both male and female mice augments firing rates by reducing the membrane potential at which APs are initiated. AP threshold is lowered due to a hyperpolarizing shift in the gating behavior of voltage-gated Na⁺ channels. Whole-cell recording also elicits a hyperpolarizing shift in the gating behavior of A-type K⁺ channels which contributes to increased firing rates. Hodgkin–Huxley modeling and pharmacological experiments reveal that gating shifts in A-type K⁺ channel activity do not impact AP threshold, but rather promote channel inactivation which removes restraint on the upper limit of firing rates. Taken together, our work reveals an unappreciated impact of voltage-gated Na⁺ channels that work in coordination with A-type K⁺ channels to regulate the firing frequency of cerebellar SCs.

Key words: A-type potassium channel; action potential; cerebellum; computational modeling; sodium channel; stellate cell

Significance Statement

The cerebellum is a brain region that fulfills critical roles in motor function in adults as well as being linked to neurodevelopmental disorders in the developing brain. Significant attention has been directed toward understanding connectivity within the cerebellum and how its neuronal circuits are regulated. Stellate cells (SCs) are inhibitory GABAergic interneurons that make-up neuronal circuits that control the output from the cerebellar cortex by regulating the firing properties of Purkinje cells. The strength of GABAergic inhibition of Purkinje cells is governed by the excitability of SCs which fire action potentials (APs) at a wide range of frequencies. Our study reveals an unappreciated role of voltage-gated sodium channels that work in coordination with A-type K⁺-channels to establish SC firing rates.

Received April 1, 2019; accepted May 13, 2019; First published May 20, 2019.
The authors declare no competing financial interests.

Author contributions: R.P.D.A., J.M., A.K., and D.B. designed research; R.P.D.A., J.M., and V.S. performed research; R.P.D.A., J.M., and V.S. analyzed data; R.P.D.A., A.K., and D.B. wrote the paper.

Introduction

Cerebellar stellate cells (SCs) are GABAergic interneurons that exert inhibitory tone onto both Purkinje cells (PCs) and SCs to shape motor function in awake, behaving animals (Astorga et al., 2017; Gaffield and Christie, 2017). Investigations into the physiologic activity of SCs both *in vitro* and *in vivo* have estimated their action potential (AP) firing rates to be in the range of 5–30 Hz (Armstrong and Rawson, 1979; Midtgaard, 1992; Häusser and Clark, 1997; Carter and Regehr, 2002), with some studies reporting even lower spontaneous rates (Jörntell and Ekerot, 2003; Liu et al., 2014). SCs are also highly sensitive to minimal amounts of synaptic input (Carter and Regehr, 2002; Jörntell and Ekerot, 2003), suggesting that the excitability of SCs is finely tuned to ensure that their target cells receive robust and reliable feedforward inhibition.

Several molecular mechanisms have been shown to modulate the excitability of SCs. For example, elevations in cytosolic Ca^{2+} mediated by T-type voltage gated Ca^{2+} channels (VGCCs) have been shown to dynamically regulate the firing rates of SCs by modulation of somatodendritic A-type K^+ channels (Molineux et al., 2005; Anderson et al., 2013). Firing rates are further controlled by neurochemical transmission. The inhibitory tone of GABA_A receptors constrains AP firing (Häusser and Clark, 1997) whereas the prolonged depolarization by NMDA-type ionotropic glutamate receptors (Liu et al., 2014) activates axonal VGCCs (Christie and Jahr, 2008) and promotes GABA release (Glitsch and Marty, 1999; Duguid and Smart, 2004; Liu and Lachamp, 2006). To complicate matters, the firing rates of SCs are also affected by patch-clamp recording conditions. The intrinsic excitability of SCs increases in a time-dependent manner in cell-attached recordings (Alcami et al., 2012). The molecular events that give rise to this increase in excitability are still not fully understood, although observations in other cell types have demonstrated that patch breakthrough during whole-cell recording can cause unintended changes to ion channel gating and activity, including an effect on voltage-gated Na^+ channels (Fenwick et al., 1982; Dani et al., 1983; Fernandez et al., 1984; Vandenberg and Horn, 1984; Townsend et al., 1997). Whether a similar mechanism accounts for increased firing in SCs in whole-cell recordings has yet to be investigated.

Here, we have elucidated the molecular events responsible for the increase in excitability of SCs in whole-cell

recording conditions. Using a combination of brain slice patch-clamp electrophysiology and Hodgkin–Huxley modeling, we show that shifts in the gating properties of voltage-gated Na^+ channels cause an increase in SC excitability by promoting AP firing at more hyperpolarized potentials. These events occur concurrently with a hyperpolarizing shift in A-type K^+ channel gating which reduces the number of channels available for activation, and thus contributes to increased AP firing. Taken together, our data identify an unappreciated role of voltage-gated Na^+ channels that work in coordination with somatodendritic A-type K^+ channels to upregulate SC excitability on whole-cell recording.

Materials and Methods

Ethical approval

All experiments have been approved by the Animal Care Committee of McGill University and were performed in accordance with the guidelines of the Canadian Council on Animal Care.

Animals

Wild-type mice with a C57BL/6J background (RRID: IMSR_JAX:000664) were obtained from The Jackson Laboratory and maintained as a breeding colony at McGill University. Both male and female wild-type mice were used for experiments and ranged from postnatal day 18 to 30.

Slice preparation

Mice were anesthetized with isoflurane and immediately decapitated. A block of cerebellar vermis was rapidly dissected from the mouse head and submerged in ice-cold cutting solution perfused with carbogen gas (95% O_2 , 5% CO_2). Cutting solution contains: 235 mM sucrose, 2.5 mM KCl, 1.25 mM NaH_2PO_4 , 28 mM NaHCO_3 , 0.5 mM CaCl_2 , 7 mM MgCl_2 , 28 mM D-glucose, 1 mM ascorbic acid, and 3 mM sodium pyruvate (pH 7.4; 305–315 mOsmol/l). The block of vermis is then fastened to a platform, transferred to the slicing chamber and again submerged in ice-cold cutting solution, bubbled with carbogen throughout the remainder of the procedure. Thin slices of cerebellar vermis (300 μm) were obtained with a vibrating tissue sectioner (Leica VT1200; Leica Instruments). The slices were transferred to oxygenated artificial CSF (aCSF) and held at room temperature (21°C–23°C) for at least 1 h before recordings were performed. aCSF contained the following: 125 mM NaCl, 2.5 mM KCl, 1.25 mM NaH_2PO_4 , 26 mM NaHCO_3 , 2 mM CaCl_2 , 1 mM MgCl_2 , and 25 mM D-glucose (pH 7.4; 305–315 mOsmol/l).

Electrophysiology

Slice experiments were performed on an Olympus BX51 upright microscope (Olympus) equipped with differential interference contrast/infrared optics. Whole-cell patch-clamp recordings were made from visually-identified stellate, granule or Purkinje cells in acute sagittal slices of cerebellar vermis. SCs were distinguished from misplaced or migrating granule, glial or basket cells by their small soma diameter (8–9 μm), location in the

This work was supported by the Canadian Institutes of Health Research Operating Grant MOP 142431 (to D.B.) and by a National Natural Sciences and Engineering Research Council of Canada (NSERC) Discovery Grant (A.K.). R.P.D.A. was supported by a NSERC CGS-D Doctoral Fellowship.

Acknowledgements: We thank members of the Bowie laboratory for comments on this manuscript and Z. Nusser for discussions on sodium channel expression patterns.

Correspondence should be addressed to Derek Bowie at derek.bowie@mcgill.ca. <https://doi.org/10.1523/ENEURO.0126-19.2019>

Copyright © 2019 Alexander et al.

This is an open-access article distributed under the terms of the Creative Commons Attribution 4.0 International license, which permits unrestricted use, distribution and reproduction in any medium provided that the original work is properly attributed.

outer two-thirds of the molecular layer and whole-cell capacitance measurement (4–12 pF). Granule cells (GCs) were identified based on location in the granule layer (immediately less superficial to the Purkinje layer), small soma size and whole-cell capacitance measurement (1–3 pF). Purkinje cells were identified based on large relative size, location in the Purkinje monolayer and whole-cell capacitance measurement (25–35 pF). Patch pipettes were prepared from thick-walled borosilicate glass (GC150F-10, OD 1.5 mm, ID 0.86 mm; Harvard Apparatus Ltd) and had open tip resistances of 4–7 M Ω when filled with an intracellular recording solution. Recordings were performed using a Multiclamp 700A amplifier (Molecular Devices) at a holding potential of –70 mV (stellate and Purkinje) or –80 mV (granule). Series resistance and whole-cell capacitance were estimated by cancelling the fast transients evoked at the onset and offset of brief (10 ms) 5-mV voltage-command steps. Access resistance during whole-cell recording (7–25 M Ω) was compensated between 60 and 80% and checked for stability throughout the experiments (~15% tolerance). Recordings where pipette offset changed by >3 mV were excluded. Liquid junction potential was not corrected for. The bath was continuously perfused at room temperature (21°C–23°C) with aCSF at a rate of 1–2 mL/min. Currents were filtered at 5 kHz with an eight-pole low-pass Bessel filter (Frequency Devices) and digitized at either 25 or 100 kHz with a Digidata 1322A data acquisition board and Clampex 10.1 (pClamp, RRID:SCR_011323) software. For voltage-clamp recordings, the online P/N leak-subtraction suite in Clampex 10.1 was used to assess voltage-gated responses.

For recording voltage dependence of activation of A-type K⁺ current (I_A) a protocol was applied consisting of 500-ms steps evoked from a holding potential of –100 mV, ranging from –100 to +20 mV in 10-mV increments. An inactivation protocol was applied consisting of 500-ms prepulse steps ranging from –120 to –30 mV in 5-mV increments, followed by a probe step to –20 mV to assess channel availability. For recording voltage dependence of activation of delayed rectifier K⁺ current (I_K), a protocol was applied consisting of 1-s steps evoked from a holding potential of –50 mV, ranging from –50 to +40 mV in 5-mV increments. The holding potential of –50 mV was chosen to selectively inactivate I_A , because of its relatively hyperpolarized $V_{1/2}$ inactivation, and study a more isolated I_K . For recording voltage dependence of activation of Na⁺ current (I_{Na}), a protocol designed to circumvent space-clamp errors in neurons was used (Milescu et al., 2010) consisting of a 5-ms suprathreshold step from –80 to –35 mV to evoke an action current, followed by a ~1-ms step to –60 mV, followed by 100-ms steps ranging from –80 to +30 mV in 5-mV increments. To measure steady-state channel availability, an inactivation protocol consisting of 100-ms steps ranging from –110 to –20 mV in 5-mV increments, followed by a probe step to –20 mV.

Recording solutions

All chemicals were obtained from Sigma Aldrich unless otherwise indicated. Internal pipette solution for most

current-clamp experiments as well as voltage-clamp experiments, both whole-cell and nucleated patch, examining I_K in SCs contained: 126 mM K-gluconate, 5 mM HEPES, 4 mM NaCl, 15 mM D-glucose, 0.05 mM CaCl₂, 1 mM MgSO₄, 0.15 mM K₄-BAPTA, 2 mM Mg-ATP, and 0.1 mM Na-GTP (adjusted to pH 7.4 with KOH, 300–310 mOsmol/l). I_K experiments had external aCSF supplemented with 100 nM tetrodotoxin (TTX) to block AP firing, as well as 5 mM 4-aminopyridine (4-AP) to limit the activity of I_A -mediating channels. In one set of experiments, all K-gluconate in this internal solution was substituted for K-methanesulfonate to examine the effect of different anions on intrinsic membrane properties. Pipette solution for voltage-clamp experiments, both whole-cell and nucleated patch, examining I_A contained: 140 mM KCl, 10 mM HEPES, 2.5 mM MgCl₂, and 0.15 mM K₄-BAPTA (adjusted to pH 7.4 with KOH, 300–310 mOsmol/l). For these experiments, the external aCSF was supplemented with 5 mM TEA-Cl and 2 mM CsCl to block non- I_A -mediating K⁺ channels, and 100 nM TTX to block AP firing. Pipette solution for voltage-clamp experiments examining I_{Na} contained: 110 mM Cs-methanesulfonate, 5 mM HEPES, 4 mM NaCl, 15 mM D-glucose, 0.05 mM CaCl₂, 0.15 mM Cs₄-BAPTA, 4 mM Mg-ATP, 0.1 mM Na-GTP, 10 mM TEA-Cl, and 10 mM 4-AP (adjusted to pH 7.4 with CsOH, 300–310 mOsmol/l). Pipette solution for voltage-clamp experiments examining I_{Na} in excised membrane patches contained: 140 mM CsCl, 10 mM HEPES, 10 mM EGTA, 2 mM MgCl₂, and 2 mM Na₂-ATP (adjusted to pH 7.4 with CsOH, 300–310 mOsmol/l). Free Ca²⁺ concentration for all current-clamp internal solutions was calculated to be ~100 nM using MaxChelator freeware (Bers et al., 2010). For all experiments investigating I_{Na} , the external aCSF was supplemented with 100 μ M CdCl₂ and 1 μ M Mibefradil dihydrochloride (Tocris Bioscience) to block voltage-gated calcium channels. Additional current-clamp experiments were performed in the presence of hyperpolarization-activated cyclic nucleotide-gated channel (HCN) blocker ZD 7288 in the aCSF (20 μ M; Tocris Bioscience). Except where indicated, all experiments were performed in the presence of fast excitatory and inhibitory synaptic blockers: NMDA receptor antagonist D-(–)-2-amino-5 phosphonopentanoic acid (D-APV; 10 μ M), AMPA/kainate receptor antagonist 2,3-dioxo-6-nitro-1,2,3,4-tetrahydrobenzo[f]quinoxaline-7-sulfonamide (NBQX; 10 μ M), and GABA_A receptor antagonist bicuculline (BIC; 10 μ M), all of which were purchased from Abcam.

Mathematical model

A modified Hodgkin–Huxley type model was adopted from Molineux et al. (2005) and Anderson et al. (2010). The model consists of five ionic currents, including I_{Na} , I_K , I_A , T-type Ca²⁺ current (I_T) and nonspecific leak current (I_L). The A-type K⁺ and T-type Ca²⁺ current were added in Molineux et al. (2005) to capture biphasic first spike latency profile. The resulting voltage equation associated with this model is expressed as

$$C_m \frac{dV}{dt} = -[I_{Na} + I_K + I_A + I_T + I_L] + I_{app},$$

where C_m is the membrane capacitance per unit area and I_{app} is the applied current. The kinetics of the various ionic currents included in the model are as described below (Molineux et al., 2005; Anderson et al., 2010).

(1) Fast activating Na^+ current:

$$I_{Na} = \bar{g}_{Na} m_{\infty}^3 h (V - V_{Na}),$$

with maximum conductance \bar{g}_{Na} and Nernst potential for Na^+ V_{Na} . Its gating is governed by both the steady state activation function

$$m_{\infty} = (1 + e^{-(V-v_m)/s_m})^{-1}$$

and the inactivation variable h satisfying the dynamic equation

$$\frac{dh}{dt} = \frac{h_{\infty}(V) - h}{\tau_h(V)},$$

where $h_{\infty}(V)$ is the steady state inactivation function given by

$$h_{\infty} = (1 + e^{(V-v_h)/s_h})^{-1}$$

and $\tau_h(V)$ is its time constant described by the Lorentzian function

$$\tau_h(V) = y_0 + \frac{2Aw}{4\pi(V - V_c)^2 + w^2}.$$

(2) Delayed rectifier K^+ current:

$$I_K = \bar{g}_K n^4 (V - V_K),$$

with maximum conductance \bar{g}_K and Nernst potential for K^+ V_K . The gating of this current is governed by the activation variable n only, which satisfies the dynamic equation

$$\frac{dn}{dt} = \frac{n_{\infty}(V) - n}{\tau_n(V)},$$

where $n_{\infty}(V)$ is the steady state activation function given by

$$n_{\infty} = (1 + e^{-(V-v_n)/s_n})^{-1}$$

and $\tau_n(V)$ is its time constant defined by

$$\tau_n(V) = \frac{6}{1 + e^{(V+23)/15}}.$$

(3) A-type K^+ current:

$$I_A = \bar{g}_A n_A h_A (V - V_K)$$

with maximum conductance \bar{g}_A and Nernst potential V_K . Its activation/inactivation kinetics are governed by the

gating variables n_A and h_A , respectively, each satisfying the dynamic equations

$$\frac{dn_A}{dt} = \frac{n_{A,\infty}(V) - n_A}{\tau_{n_A}}$$

and

$$\frac{dh_A}{dt} = \frac{h_{A,\infty}(V) - h_A}{\tau_{h_A}}$$

where $n_{A,\infty}$ and $h_{A,\infty}$ are, respectively, the steady state activation and inactivation functions given by

$$n_{A,\infty} = (1 + e^{-(V-v_{n_A})/s_{n_A}})^{-1} \quad (1)$$

and

$$h_{A,\infty} = (1 + e^{(V-v_{h_A})/s_{h_A}})^{-1}$$

and τ_{n_A} and τ_{h_A} are their corresponding time constants that are independent of membrane voltage V .

(4) Fast activating T-type Ca^{2+} current:

$$I_T = \bar{g}_T m_{T,\infty} h_T (V - V_{Ca}),$$

with maximum conductance \bar{g}_T and Nernst potential for Ca^{2+} V_{Ca} . Its gating is governed by the steady state activation function

$$m_{T,\infty} = (1 + e^{-(V-v_{m_T})/s_{m_T}})^{-1}$$

and the inactivation variable h_T satisfying the dynamic equation

$$\frac{dh_T}{dt} = \frac{h_{T,\infty}(V) - h_T}{\tau_{h_T}},$$

where $h_{\infty}(V)$ is the steady state inactivation function given by

$$h_{T,\infty} = (1 + e^{(V-v_{h_T})/s_{h_T}})^{-1}$$

and τ_{h_T} is its voltage-independent time constant.

(5) Non-specific leak current:

$$I_A = \bar{g}_L (V - V_L)$$

with constant maximum conductance \bar{g}_L and Nernst potential V_L .

The model is thus described by a six-dimensional system representing the time-dependent membrane voltage V and the five time-dependent gating variables $m, n, n_A, h_A,$ and h_T .

Model parameter values

Simulations of the model using parameter values listed in Molineux et al. (2005) and Anderson et al. (2010) produced cycles of APs in the $(V, dV/dt)$ - plane that did not match the activities at either baseline (0 min) or the activities after the increase in excitability (data not shown). To capture the dynamics of the increase in excitability, we

Table 1. Parameter values of ionic currents included in the baseline and revised models whenever two values are provided for a given parameter, the first corresponds to the baseline model (before the increase in excitability at baseline) while the second shown between parentheses corresponds to the revised model (after the increase in excitability at 25 min)

Parameter	Value/units	Parameter	Value/units	Parameter	Value/units	Parameter	Value/units
C_M	1.50148 $\mu\text{F}/\text{cm}^2$	V_{Ca}	22 mV	w	46 mV	v_{m_T}	- 50 mV
\bar{g}_{Na}	3.4 $\mu\text{S}/\text{cm}^2$	V_L	- 38 mV	V_c	- 74 mV	s_{m_T}	3 mV
\bar{g}_K	9.0556 $\mu\text{S}/\text{cm}^2$	v_m	- 37 (- 44) mV	v_n	- 23 mV	v_{h_T}	- 68 mV
\bar{g}_A	15.0159 $\mu\text{S}/\text{cm}^2$	s_M	3 mV	s_n	5 mV	s_{h_T}	3.75 mV
\bar{g}_T	0.45045 $\mu\text{S}/\text{cm}^2$	v_h	- 40(- 48.5) mV	v_{n_A}	- 27(- 41) mV	τ_{n_A}	5 ms
\bar{g}_L	0.07407 $\mu\text{S}/\text{cm}^2$	s_h	4 mV	s_{n_A}	13.2 mV	τ_{h_A}	10 ms
V_{Na}	55 mV	y_0	0.1 ms	v_{h_A}	- 80(- 96) mV	τ_{h_T}	15 ms
V_K	- 80 mV	A	322 ms mV	s_{h_A}	6.5(9.2) mV		

first fitted the expressions of $n_{A,\infty}$ and $h_{A,\infty}$ to the steady state activation/inactivation kinetic data of I_A before and after the shift, then used the full model to manually fit its numerical simulations to baseline data before the increase in excitability. This was done in two sequential steps: (1) by first capturing all features of the AP cycles in the $(V, dV/dt) -$ plane at baseline, followed by (2) matching the firing frequency obtained from the temporal profiles of membrane voltage. We will refer to this model associated with baseline data as the “baseline” model. To capture all features of the AP cycle after the increase in excitability (i.e., after 25 min), we identified the list of all parameters that need to be adjusted to produce these features in the $(V, dV/dt) -$ plane and the higher firing frequency. Because our analysis revealed that the T-type Ca^{2+} current played a minor role in inducing the increase in excitability within the model, we left the kinetic parameters of activation/inactivation of I_T listed in [Molineux et al. \(2005\)](#) and [Anderson et al. \(2010\)](#) unchanged for both before and after the increase in excitability. The reversal potentials of Na^+ , K^+ and Ca^{2+} were also left unchanged. As for the remaining parameters, they were estimated based on fitting and parsimony. The resulting model that produced the increase in excitability will be referred to hereafter as “revised” model. The list of all parameter values for the baseline and revised models are provided in [Table 1](#). Simulations were run in Mathematica 11.2 (Wolfram Mathematica, RRID:SCR_014448).

Experimental design and statistical analysis

Paired t tests were used to compare electrophysiological data recorded at baseline and after 25 min (step-evoked AP frequency, AP threshold, AP cycle parameters, $V_{1/2}$ values for I_{Na}). In the cases of I_A and I_K gating properties, a two-way mixed design ANOVA was used with Tukey’s *post hoc* test to compare patch configuration data (nucleated and whole-cell) between groups while comparing data over time (baseline and 25 min) within each group. For each experimental group, recordings from a minimum of five cells from a minimum of three animals were collected. Analysis was not blinded.

Voltage dependence of activation for all current types was analyzed by first calculating conductance (G) values from the peak currents elicited by each respective activation protocol using the formula:

$$G_x = \frac{I_x}{V_m - V_{rev_x}}$$

where I_x is the peak current of current type x (i.e., I_A, I_K, I_{Na}) evoked at membrane potential V_m , and V_{rev_x} is the reversal potential of current type x . Conductance-voltage relationships for each current type were then fit to a Boltzmann function using the formula:

$$G_x = \frac{G_{max}}{1 + \exp((V_{1/2} - V_m)/k)}$$

where G_x is the conductance at membrane potential V_m for current type x , G_{max} is the maximum conductance for current type x , $V_{1/2}$ is the membrane potential where G_x is 50% of G_{max} , and k is the slope factor. Boltzmann fits were performed for each time point in each cell to calculate normalized conductance values. Summary conductance-voltage relationships for each current type were calculated by averaging the normalized conductance values across all cells in the dataset. $V_{1/2}$ values reported in the Results section for each current type were calculated by fitting the normalized conductance averages.

Data are reported as mean \pm SEM. Significance was denoted with $*p < 0.05$, $**p < 0.01$, and $***p < 0.001$. All fitting was performed with Origin 7.0 (Microcal Origin, RRID:SCR_002815). Statistical analyses were performed using SPSS 17.0 (SPSS, RRID:SCR_002865).

Results

AP firing in cerebellar stellate and GC (granule cell), but not Purkinje cells, increases during whole-cell recording

To examine time-dependent changes in membrane excitability, whole-cell patch-clamp recordings were obtained from three types of visually-identified cerebellar neurons, namely stellate, granule and Purkinje cells ([Fig. 1A–C](#)). After obtaining the whole-cell current-clamp configuration, negative current was injected into each neuron to maintain the membrane potential at -70 or -80 mV (see Materials and Methods). To assess membrane excitability following breakthrough, incremental depolarizing current steps were applied within the first minute (termed baseline), and then once every 5 min during a typical 25-min recording ([Fig. 1A–F](#)).

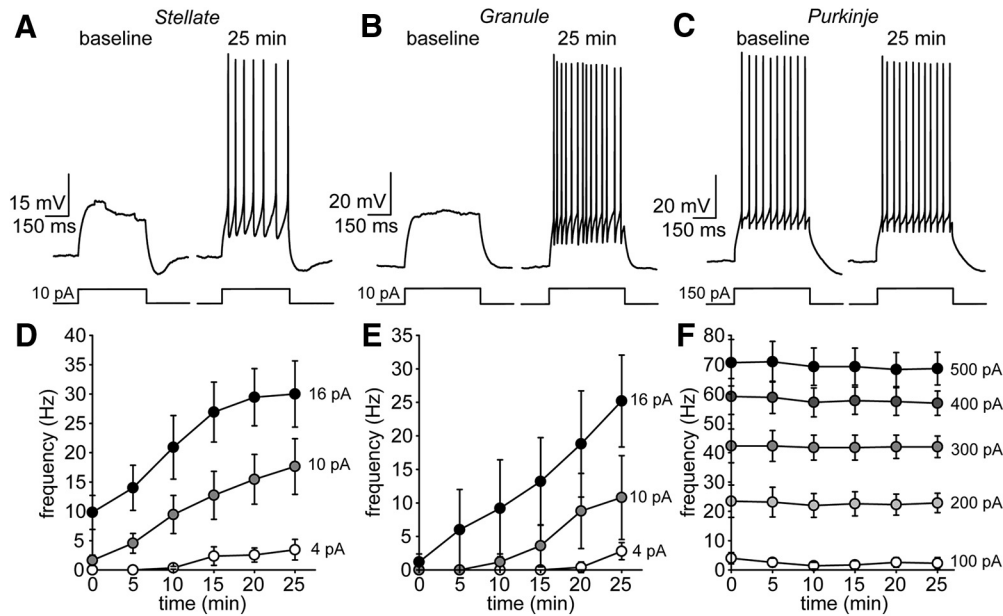


Figure 1. Stellate and GC (granule cell), but not Purkinje cells, exhibit excitability increases during whole-cell recording. **A**, Example SC current-clamp recording (patch #150129p2) applying a 10-pA step protocol shortly following breakthrough and after 25 min. **B**, **C**, Same for GC (patch #150324p2) and Purkinje cell (patch #141010p5) examples using 10- and 150-pA current steps, respectively. **D**, Summary SC AP frequency over 25-min recording for multiple step amplitudes ($n = 11$ cells). **E**, **F**, Same for granule ($n = 6$ cells) and Purkinje cells ($n = 6$ cells).

Under these conditions, both stellate and GCs fired many more APs at the 25-min time point (Fig. 1D,E). For example, in SCs, AP frequency evoked by a 16-pA current step at baseline was 9.8 ± 2.9 Hz versus 30.0 ± 5.6 Hz after 25 min ($t = 4.73, p < 0.001; n = 11$ cells; Fig. 1A,D). In contrast, firing rates in Purkinje cells remained stable throughout the recording (Fig. 1C,F) but required larger step depolarizations to elicit APs. For example, AP frequency evoked by a 400-pA step at baseline was 59.1 ± 6.1 Hz versus 56.9 ± 4.2 Hz after 25 min ($t = -0.88, p = 0.41; n = 7$ cells). The increase in AP frequency in SCs was not accompanied by a change in input resistance (1011 ± 148 M Ω at baseline vs 967 ± 137 M Ω at 25 min; $t = -1.21, p = 0.26; n = 11$ cells) or resting membrane potential (-50.6 ± 1.3 mV at baseline vs -52.2 ± 1.6 mV at 25 min; $t = -1.33, p = 0.23; n = 7$ cells) suggesting that the increase in membrane excitability was primarily due to changes in the activity of active membrane conductances (i.e., ion channels). In contrast, the increase in step-evoked AP frequency in GCs (16-pA step: 1.2 ± 1.2 Hz at baseline vs 25.2 ± 6.7 Hz at 25 min; $t = 4.07, p = 0.015; n = 5$ cells; Fig. 1B,E) was accompanied by a concurrent increase in membrane input resistance ($44.5 \pm 13.4\%$ increase, $n = 3$ cells). Given this, we focused the rest of our study on SCs to pinpoint the molecular events that give rise to the increase in membrane excitability.

A closer examination of SC recordings revealed a decrease in spike latency in response to current injection (Fig. 2A) at all current step amplitudes tested (Fig. 2B). For example, the latency to first spike in response to a 16-pA current step at baseline was 89.9 ± 14.4 versus 37.1 ± 9.5 ms at 25 min ($t = -6.68, p < 0.001; n = 11$ cells). To measure the shift precisely, we used a 1-s current ramp

protocol to monitor the membrane potential at the initiation of the AP upstroke. To ensure that the ramp protocol had no direct effect on spike threshold, the protocol began with a 5-pA ramp that increased five times in increments of 5 pA. The threshold for each cell was then calculated by averaging the value obtained at each ramp amplitude. For comparison, we also repeated these experiments on both granule (not shown) and Purkinje cells (Fig. 2D,E). As anticipated, SCs exhibited a shift in AP threshold starting at -39.7 ± 0.9 mV following breakthrough and hyperpolarizing to -48.2 ± 1.3 mV at 25 min ($t = -15.74, p < 0.001; n = 12$ cells; Fig. 2C,E). GCs exhibited an even more substantial hyperpolarizing shift in AP threshold (-35.9 ± 0.6 mV at baseline vs -52.5 ± 2.1 mV at 25 min; $t = -7.31, p < 0.001; n = 6$ cells) whereas the threshold in Purkinje cells remained constant (-48.5 ± 1.5 mV at baseline vs -49.5 ± 1.4 mV at 25 min; $t = -0.073, p = 0.51; n = 5$ cells; Fig. 2E).

To ensure that the excitability increase in SCs was present in physiologically relevant conditions, the temperature of the aCSF perfusion was raised to near-physiologic level (33°C–34°C) and current-clamp experiments were repeated. SCs at elevated ambient temperatures still exhibited hyperpolarizing AP thresholds that closely resembled those at room temperature (-37.4 ± 1.7 mV at baseline vs -47.4 ± 1.9 mV at 20 min; $t = 10.04, p < 0.001; n = 5$ cells). Lastly, since others have noted that internal anions can affect intrinsic membrane properties of neurons during whole-cell recording (Kaczorowski et al., 2007), we repeated current-clamp experiments in SCs using a K-methanesulfonate-based intracellular solution in place of the initial K-gluconate version. Although slightly hyperpolarized at baseline compared to gluconate, the pres-

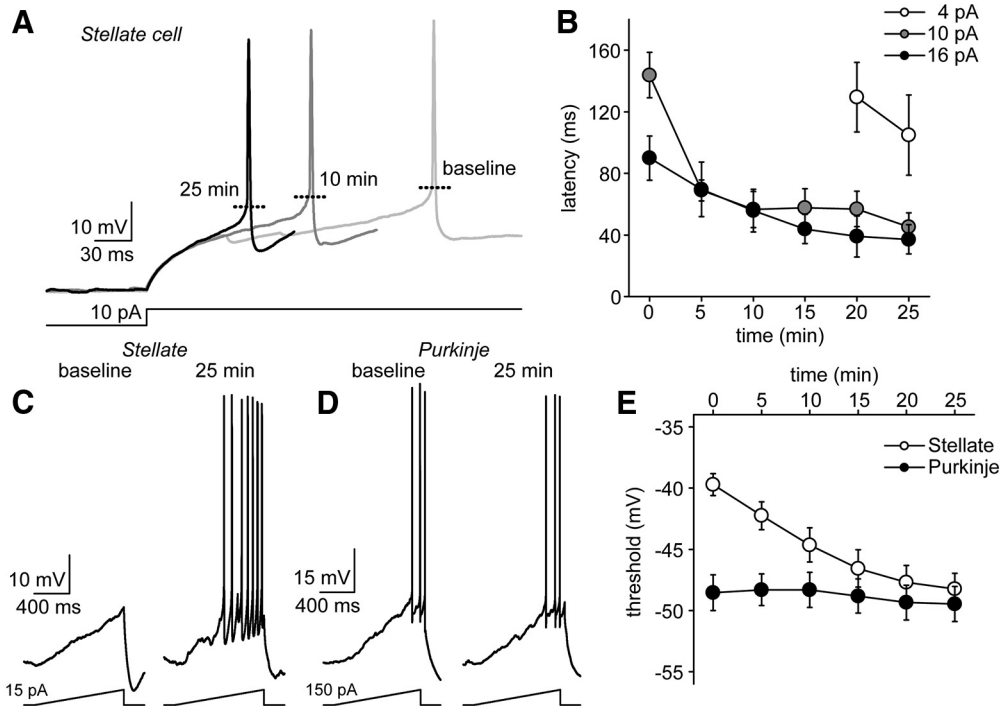


Figure 2. Excitability increase is underpinned by decrease in spike latency and hyperpolarization of AP threshold. **A**, First APs fired by a SC in response to 10-pA current step at three different time points: 1, 10, and 25 min after breakthrough. The spike latency in response to the step decreases substantially over the course of the recording. **B**, Summary plot of spike latencies for multiple step amplitudes over the course of a 25-min recording ($n = 11$ cells). **C**, Example current-clamp responses evoked by ramp protocol at baseline (left) and after 25 min (right) in a SC (patch #150129p2). **D**, Same for an example Purkinje cell (patch #141010p5). **E**, Summary plot depicting change in AP threshold over time in stellate ($n = 11$ cells) and Purkinje cells ($n = 6$ cells).

ence of methanesulfonate did not prevent the decrease of AP threshold over the duration of patch-clamp recording (-42.8 ± 1.1 mV at baseline vs -51.0 ± 1.8 mV at recording endpoint; $t = 6.14$, $p < 0.001$; $n = 7$ cells).

Modified Hodgkin–Huxley model predicts a dominant role for voltage-gated Na⁺ channels

To better understand the change in excitability of SCs, we used a modified Hodgkin–Huxley model to examine the potential impact of ion channels that are likely to be involved. The model was based on a previous study that included a voltage-gated Na⁺ current (I_{Na}), a delayed rectifier K⁺ current (I_K), an A-type K⁺ current (I_A), a T-type Ca²⁺ current (I_T) and a leak current (I_L ; Molineux et al., 2005). The A-type K⁺ and T-type Ca²⁺ currents were specifically included in the model as they have been shown to play key roles in determining first spike latencies (Molineux et al., 2005; Anderson et al., 2010, 2013). The model parameters were then adjusted to match observations of spontaneous AP firing at the beginning of SC recordings (see Materials and Methods).

To provide an accurate experimental baseline to use as a template for modeling spontaneous AP firing, gap-free recordings from multiple SCs were made in the absence of injected current (Figs. 3, 4A). In line with the previous current step and ramp experiments, spontaneous AP firing in all SCs increased significantly over 25 min (12.5 ± 3.2 Hz at baseline vs $17.9 \pm$ Hz at 25 min; $t = 2.60$, $p = 0.041$; $n = 7$ cells; Figs. 3A, 4A). The AP cycle, which was

obtained from these data by taking the derivative of the measured voltage plotted against membrane potential (Figs. 3A, 4B), revealed two defining characteristics of time-dependent changes in AP shape: (1) a negative shift in AP upstroke, indicating the hyperpolarization of spike threshold (defined as $dV/dt = 10$ mV/ms; Fig. 3B, yellow box); (2) a reduction in the peak of the AP cycle where it intersects with the voltage-axis (Fig. 3B, green box). These measurements were compared over multiple SCs, demonstrating significant differences in AP threshold (-38.7 ± 1.3 mV at baseline vs -44.5 ± 1.7 at 25 min; $t = -11.25$, $p < 0.001$; $n = 7$ cells; Fig. 3C) as well as AP maximum (-2.7 ± 2.4 mV at baseline vs -11.5 ± 2.1 mV at 25 min; $t = -4.41$, $p = 0.0045$; $n = 7$ cells; Fig. 3C). The change in after-hyperpolarization (AHP) minimum (Fig. 3B, light blue box) was variable across cells (three examples in Fig. 3A), but this was not significant (-55.4 ± 1.3 mV at baseline vs -56.5 ± 1.5 mV at 25 min; $t = -0.88$, $p = 0.41$; $n = 7$ cells; Fig. 3C). Together, these findings identify three cardinal features that are observed during whole-cell recording from SCs: (1) an increase in spontaneous AP frequency, (2) a hyperpolarizing shift of AP threshold, and (3) a hyperpolarizing shift in the AP maximum.

To examine the potential impact of each ionic current, we systematically modified their activation and inactivation kinetic parameters in the baseline model and compared the resulting AP cycle with experimental data. For example, a symmetrical negative shift of both activation ($h_{A, \infty}$) and inactivation ($h_{A, \infty}$) functions of I_A , obtained by

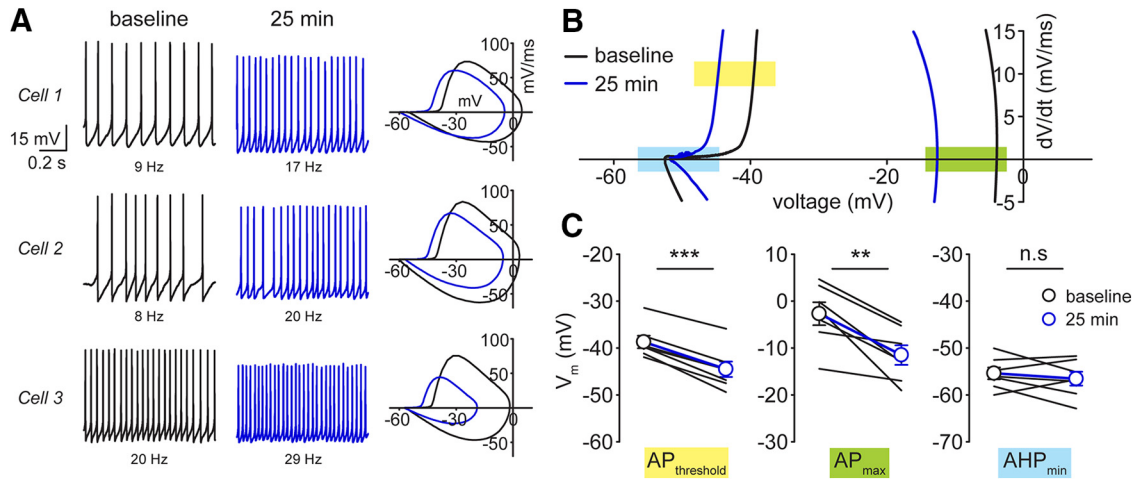


Figure 3. Defining the hallmark membrane features of SC excitability increase. **A**, left panels, Spontaneous AP firing traces from three example SCs at baseline (black) and after 25 min (blue; patch #150129p2, #181111p6, #181109p3). Right panels, AP cycles for each cell calculated from voltage-time data at baseline (black) and 25 min (blue). Colored rectangles designate quantities of interest (yellow, AP threshold; green, AP maximum; light blue, AHP minimum). **B**, AP cycle plot of an example SC with y-axis expanded. **C**, Summary comparison of these three features measured from individual AP cycles ($n = 7$ cells). *** denotes $p < 0.001$, ** denotes $p < 0.01$, n.s. denotes $p > 0.05$.

decreasing both v_{n_A} and v_{h_A} by -2.5 mV, yielded a $\sim 50\%$ increase in AP firing frequency but no change in the shape of the AP cycle (Fig. 4C). Likewise, shifts in either activation (Fig. 4D) or inactivation (Fig. 4E) functions of I_A separately showed substantial shifts in firing frequency without altering the AP cycle shape or threshold. A negative shift in the activation function (n_{∞}) of I_K , obtained by decreasing v_n by -2.5 mV, resulted in no change in AP firing frequency but produced a leftward extension of the AHP in the AP cycle (Fig. 4F). Shifting either the activation function $m_{T,\infty}$ (Fig. 4G) or inactivation function $h_{T,\infty}$ (Fig. 4H) of I_T , obtained by decreasing each v_{m_T} and v_{h_T} separately by -2.5 mV, had little effect on AP firing frequency (where only an $\sim 20\%$ increase in the former and a $\sim 20\%$ decrease in the latter were observed) and no effect on the AP cycle. Given this, we concluded that T-type Ca^{2+} channels are unlikely to contribute to the temporal increase in excitability of SCs. Although the A-type K^+ channel may contribute to the increase in AP firing rates, other ion channels must be responsible for the hyperpolarizing shift in AP threshold.

Modification of the model parameters defining I_{Na} had a substantial impact on AP firing and the AP cycle profile (Fig. 5). Identical negative shifts in both activation and inactivation parameters resulted in a concomitant shift in the AP cycle upstroke as well as an increase in AP firing frequency, although a reduction in the AP maximum was absent (Fig. 5A). Likewise, a differential left-shift in favor of the activation function (given by -5 mV for activation and -2.5 mV for inactivation) produced a $\sim 80\%$ increase in AP firing frequency, but was unable to generate a reduction in AP maximum (Fig. 5B). In contrast, a differential left-shift in favor of inactivation resulted in a $\sim 100\%$ increase in AP firing as well as reproducing the profile of the AP cycle similar to that observed experimentally (Fig. 5C). Taken together, the model suggests that hyperpolarizing shifts in

the gating properties of I_{Na} alone can account for the increase in firing rate as well as the characteristic AP cycle changes exhibited by SCs during patch-clamp recording.

SC excitability is accompanied by gating shifts in I_A but not I_K

To directly test the prediction of the model, we used customized activation and inactivation voltage-clamp protocols to isolate two subtypes of K^+ current, I_A and I_K (Figs. 6, 7; see Materials and Methods). Since it can be problematic to accurately measure voltage-gated ion channel activity in highly ramified structures such as neurons, we repeated experiments in nucleated patches where a more faithful voltage-clamp control can be achieved. In whole-cell recordings, we observed a significant time-dependent shift in the voltage dependence of both activation and inactivation of I_A (Fig. 6B,D). From Boltzmann fits of conductance-voltage relationships, $V_{1/2}$ activation of I_A shifted from -25.8 ± 2.4 mV at baseline to -39.1 ± 2.6 mV after 25 min ($F = 7.07$, $p < 0.001$, Tukey's *post hoc* test; $n = 7$ cells), while $V_{1/2}$ inactivation changed from -80.7 ± 2.8 mV at baseline to -95.3 ± 4.6 mV at 25 min ($t = -11.91$, $p < 0.001$; $n = 7$ cells). Plotting the normalized changes in $V_{1/2}$ measurements between baseline and after 25 min for individual cells yielded a comparable result ($\Delta V_{1/2}$ activation: -15.7 ± 2.7 mV; $\Delta V_{1/2}$ inactivation: -16.2 ± 1.5 mV; Fig. 6E). Since the changes in $V_{1/2}$ activation and $V_{1/2}$ inactivation are very similar, this produced a hyperpolarizing shift in the window current of about -11 mV with the midpoint moving from -62.5 to -73.5 mV (Fig. 6F). Interestingly, the shift in the voltage dependence of activation of I_A was completely lost in nucleated patches suggesting that the time-dependent change in the gating properties of I_A is probably mediated by a cytoplasmic signaling pathway, such as phosphorylation (Fig. 6G,H). The $V_{1/2}$ activation was -19.6 mV at baseline and -19.3 mV after 25 min of recording ($F = 0.07$,

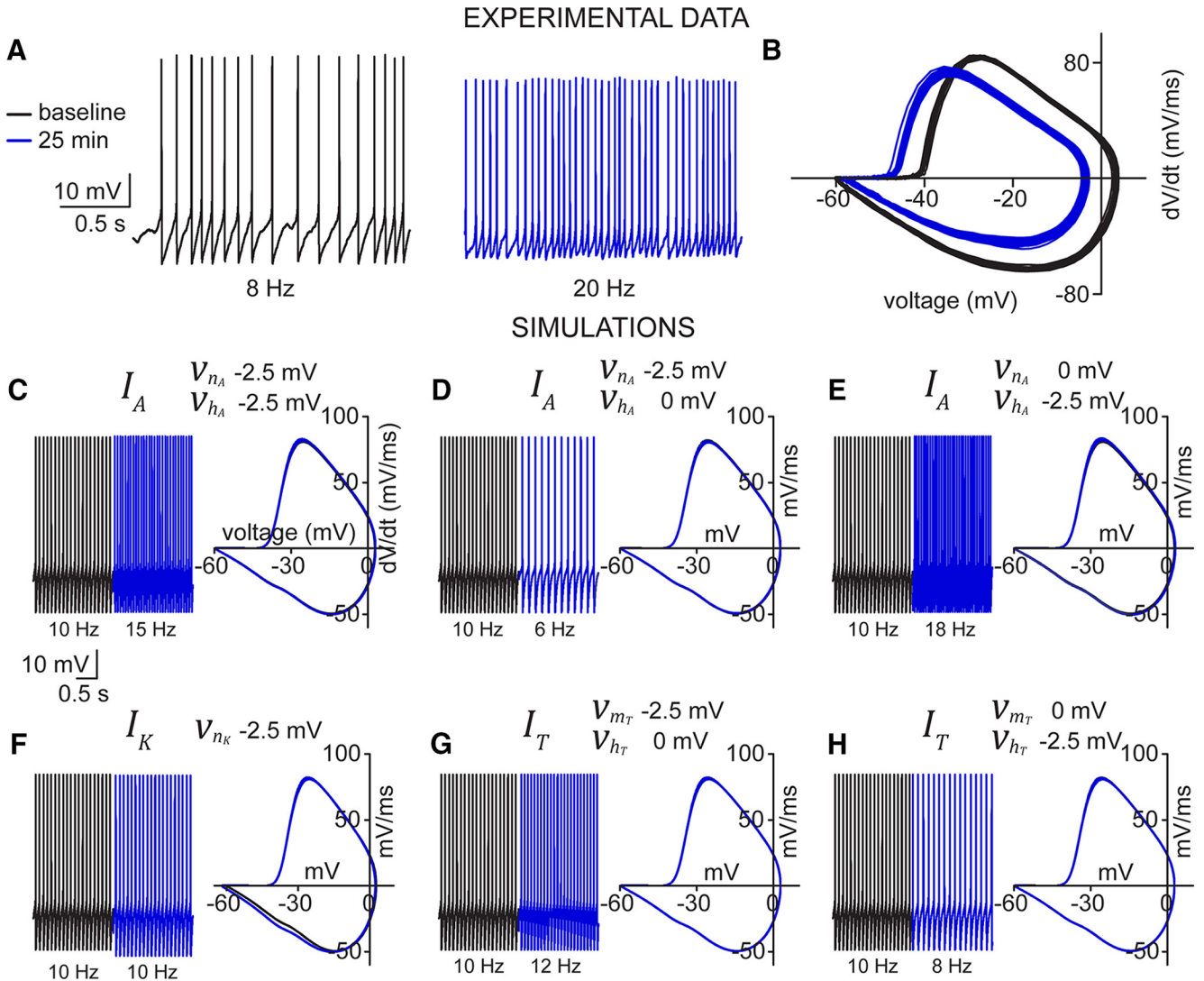


Figure 4. Simulating I_A , I_K , and I_T shifts predicts little contribution to excitability increase. **A**, Example SC current-clamp recording depicting spontaneous AP firing at baseline (black) and after 25 min (blue; patch #181111p5). **B**, AP cycle calculated from current-clamp data from **A** at baseline (black) and 25 min (blue). **C–E**, Simulated spontaneous firing and AP cycle from baseline model (black) and after making symmetric and asymmetric shifts in v_{n_A} and v_{h_A} (blue). **F**, Same for I_K after shifting v_{n_K} (blue). **G**, **H**, Same for I_T after shifting either v_{m_T} or v_{h_T} .

$p = 0.96$, Tukey’s *post hoc* test; $n = 6$ patches), which was slightly more depolarized than measurements in whole-cell recordings ($F = 3.31$, $p = 0.038$, Tukey’s *post hoc* test; Fig. 6H), possibly reflecting the improvement in voltage-clamp control.

In contrast to I_A , there was no significant time-dependent change in the voltage dependence of I_K activation in whole-cell recording, nor in nucleated patches ($F = 3.88$, $p = 0.081$, two-way mixed design ANOVA; Fig. 7A–D). In whole-cell configuration, $V_{1/2}$ activation at baseline was -17.7 mV compared to -17.5 mV at 25 min ($n = 8$ cells), while the voltage dependence of activation in excised patches ($n = 6$) was -3.6 mV at baseline compared to $+2.6$ mV at 25 min. There was, however, a significant difference in $V_{1/2}$ values between measurements made in whole-cell and nucleated patches ($F = 23.42$, $p < 0.001$, two-way mixed design ANOVA), suggesting that the recording configuration (whole-cell vs patch) affects I_K gating.

I_{Na} exhibits hyperpolarizing shifts in both activation and inactivation

Because of space clamp issues, it is not possible to record the fast gating of I_{Na} in SCs with conventional voltage-clamp protocols. The main problem is the inability to accurately record Na^+ channel activity in distant processes such as axons. To circumvent this, we adapted a protocol using a depolarizing prepulse step to inactivate Na^+ channels distant from the recording electrode which was followed shortly afterward with a second test step to record Na^+ channels close to the cell soma (Milescu et al., 2010). Using this approach, we reliably resolved well-clamped, albeit smaller, I_{Na} responses in SCs to profile their activation and inactivation properties (Fig. 8A–D). Performing this protocol over a 25 min period revealed that SC Na^+ channels undergo a hyperpolarizing shift of -7.8 mV in their activation (-32.4 ± 1.5 mV at baseline vs -40.2 ± 1.6 mV at 25 min; $t = -9.10$, $p < 0.001$; $n = 11$

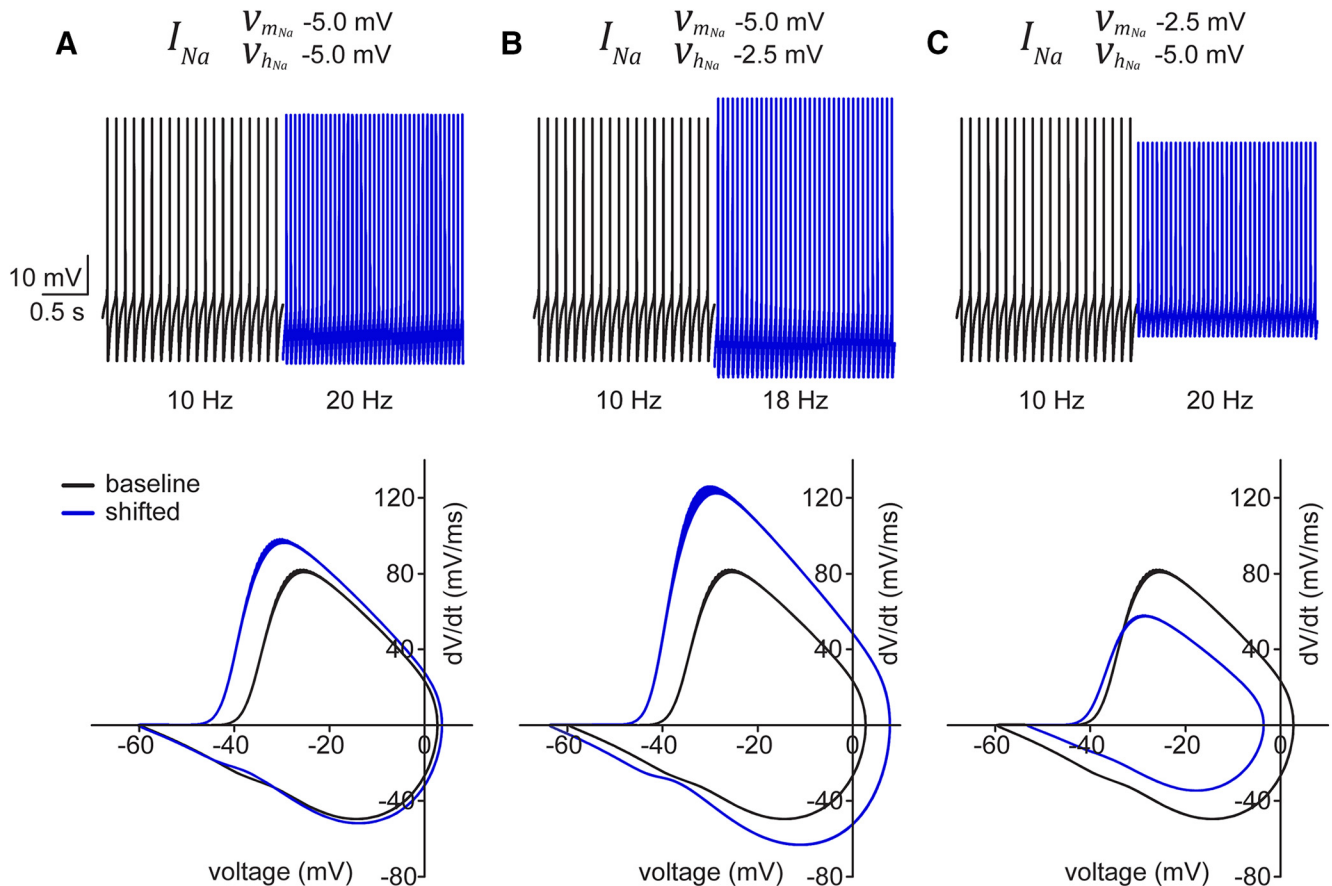


Figure 5. Simulated I_{Na} shifts suggest primary role for sodium channel in excitability increase. Simulated spontaneous firing (upper panels) and AP cycles (lower panels) from baseline model (black) and after either symmetric (**A**) or asymmetric (**B**, **C**) shifts in v_{mNa} and v_{hNa} .

cells; Fig. 8A,B) and a similar hyperpolarizing shift in steady-state inactivation (-49.3 ± 0.7 mV at baseline to -57.4 ± 1.0 mV at 25 min; $t = -8.95$, $p < 0.001$; $n = 11$ cells; Fig. 8C,D). This finding is in agreement with the hyperpolarizing shift in Na^+ channel gating predicted by the modified Hodgkin–Huxley model applied to stellate AP firing (Fig. 5).

Interestingly, we also observed a reduction in peak I_{Na} current density that developed over the duration of the experiment (-75.5 ± 8.4 pA/pF at baseline vs -45.1 ± 6.7 pA/pF at 25 min; $t = 6.64$, $p < 0.001$; $n = 11$ cells; Fig. 8E). To test whether this was due to a reduction in I_{Na} current density or a consequence of the hyperpolarizing shift in inactivation, we compared peak currents from the first step of the inactivation protocol (-110 - to -20 -mV probe; Fig. 8F). At this voltage, all SC Na^+ channels are available for activation both at baseline and after a 25-min recording. According to this measure, there is no difference between Na^+ current density before and after 25 min and this reduction reflects the shift in steady-state inactivation alone (peak current: -2012.3 ± 149.1 pA at baseline vs -1984.5 ± 162.8 pA at 25 min; $t = 0.43$, $p = 0.68$; $n = 11$ cells; Fig. 8F,G).

Pharmacological block of K^+ , Ca^{2+} , or HCN channels has no effect on AP threshold

To test the hypothesis that the shift in Na^+ channel gating is primarily responsible for the increase in SC excitability, we examined whether pharmacological block

of I_A with 4-AP attenuates the hyperpolarizing shift in AP threshold. As expected, block of I_A with bath application of 2 mM 4-AP resulted in a more depolarized inter-spike membrane potential at baseline compared to control cells (Fig. 9B). 4-AP, however, did not attenuate the shift in AP threshold (Fig. 9A) which hyperpolarized from -40.7 ± 0.9 mV at baseline to -48.6 ± 0.9 mV after 25 min ($t = -9.37$, $p < 0.001$; $n = 5$ cells). Interestingly, 2 mM 4-AP also attenuated the AHP of the AP (Fig. 9B) which may reflect pharmacological block of delayed rectifier K^+ channels. In keeping with this, block of I_K with 2 mM external tetraethylammonium (TEA) had the expected effect on AP shape at baseline but did not attenuate the shift in AP threshold (Fig. 9C,D). AP threshold observed in 2 mM TEA hyperpolarized from -37.2 ± 0.4 mV at baseline to -47.5 ± 1.4 mV after 25 min of recording ($t = -8.99$, $p < 0.001$; $n = 5$ cells; Fig. 9C,D). Since hyperpolarization-activated cyclic nucleotide-gated (HCN) channels (which mediate the mixed cation current I_h) and voltage-gated Ca^{2+} channels (VGCCs) have also been shown to affect excitability of molecular layer interneurons (MLIs; Saitow and Konishi, 2000; Anderson et al., 2010, 2013), we tested the effect of the selective I_h blocker, ZD 7288 (20 μ M) and nonselective VGCC blocker $CdCl_2$ (200 – 300 μ M) on AP threshold (Fig. 9E–H). In each case, the hyperpolarizing shift in AP threshold was unaffected by either ZD 7288 or $CdCl_2$. The AP threshold with 20 μ M ZD 7288 was -38.2 ± 1.3 mV at

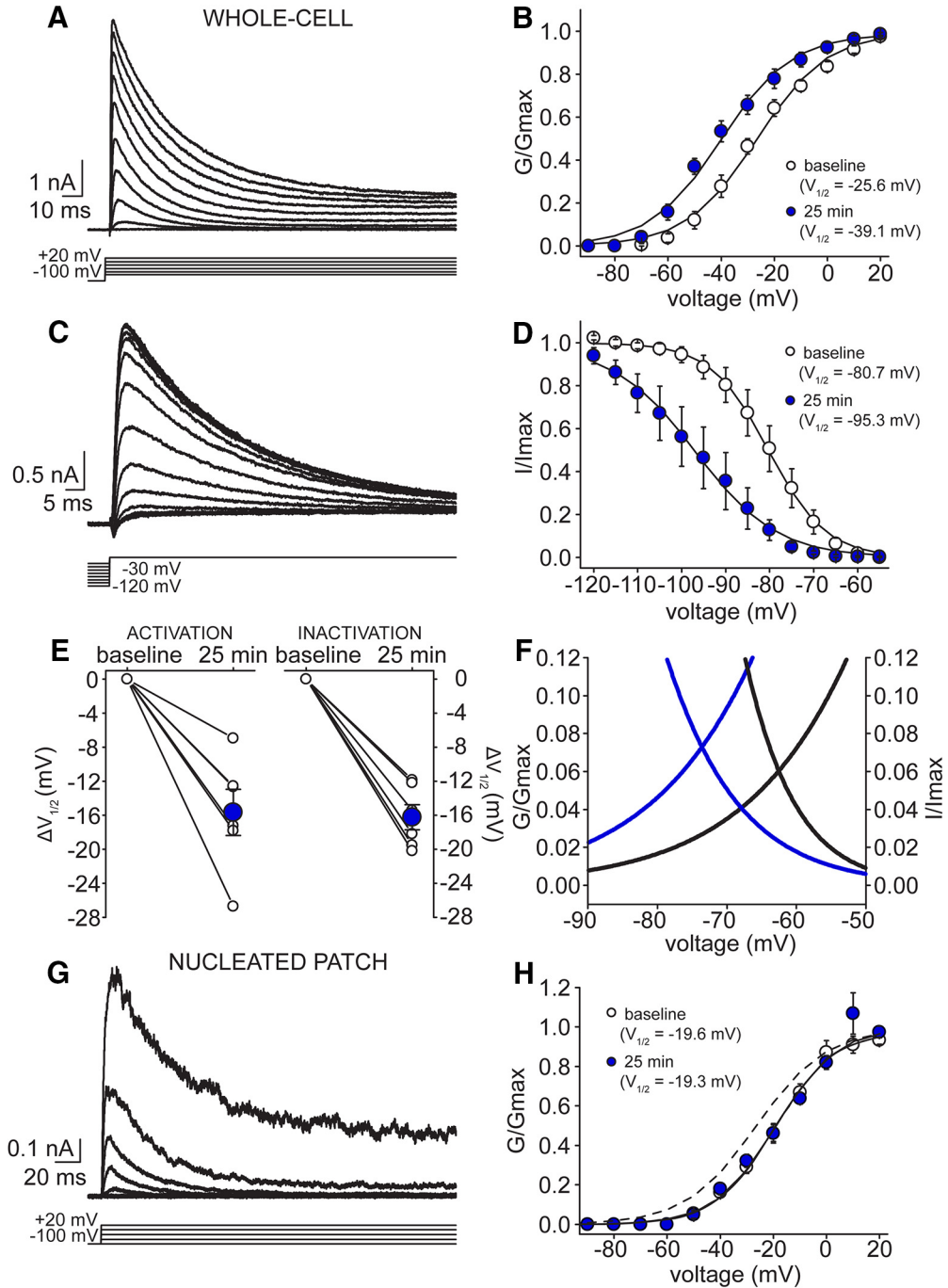


Figure 6. I_A exhibits shifts in both activation and inactivation during 25-min recording. **A**, Example voltage-clamp traces of I_A currents at baseline during activation protocol (patch #171024p3). **B**, Summary plot of voltage dependence of activation of I_A at baseline (white circles) and after 25 min of recording (blue circles; $n = 7$ cells). **C**, Example voltage-clamp traces of I_A currents evoked during inactivation protocol (patch #171127p3). **D**, Summary plot of voltage dependence of inactivation of I_A at baseline (white circles) and after 25 min of recording (blue circles; $n = 7$ cells, same as in **B**). **E**, Normalized $V_{1/2}$ activation (left) and inactivation (right) compared to delta shift after 25-min recording for each cell (white circles), along with summary mean delta for each measure (blue circles). **F**, Zoom-in of Boltzmann fits for both voltage dependence of activation and inactivation at baseline (black lines) and at 25 min (blue lines) from **B**, **D**, respectively, depicting symmetrical translocation of I_A window current. **G**, Example voltage-clamp traces of I_A currents during activation protocol observed in a SC nucleated patch (patch #180510p3). **H**, Summary plot of voltage dependence of activation of I_A at baseline (white circles) and 25 min (blue circles; $n = 6$ patches). Dashed line depicts baseline activation curve measured in whole-cell configuration from **B**.

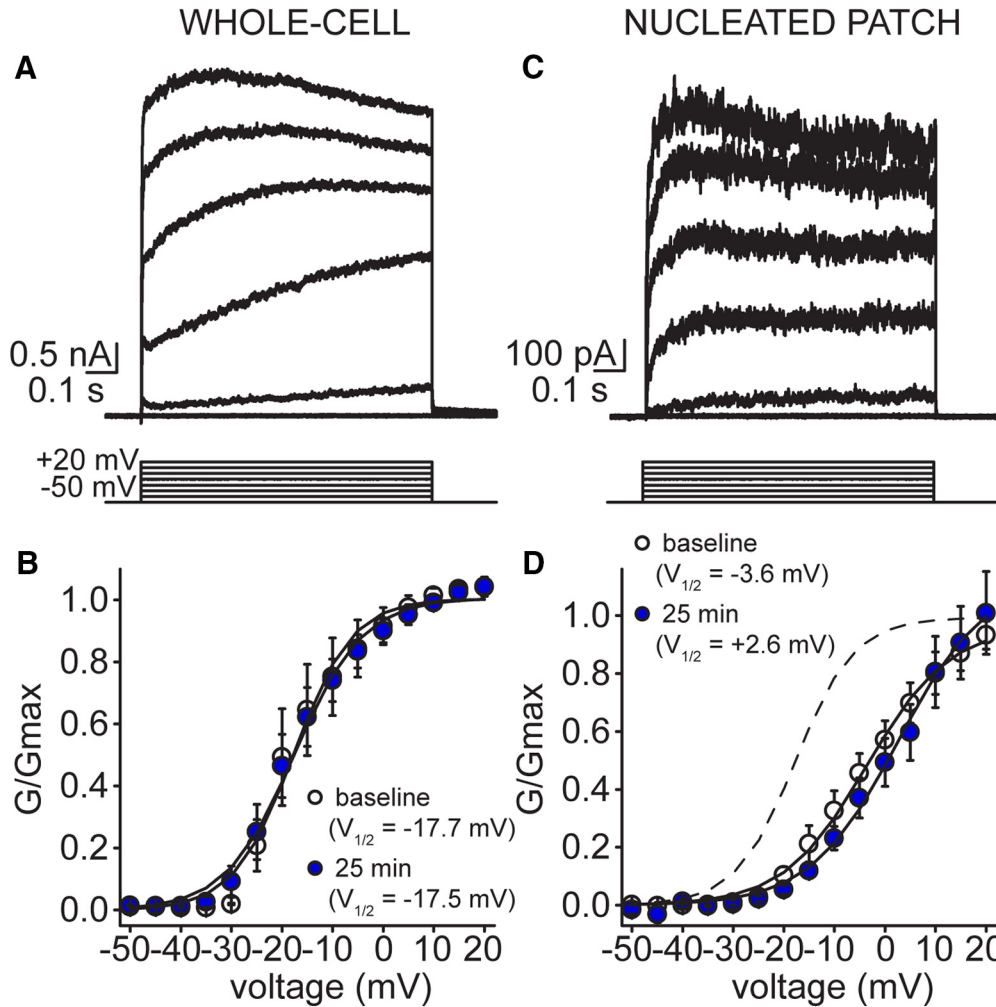


Figure 7. I_K voltage dependence of activation remains stable over patch-clamp recording in both whole-cell and nucleated patch configurations. **A**, Example whole-cell voltage-clamp traces of delayed rectifier K^+ current at baseline during activation protocol evoked from -50 -mV holding potential (5-mV increments, up to $+20$ mV; patch #180521p2). **B**, Summary plot of voltage dependence of activation of delayed rectifier K^+ current at baseline (white circles) and after 25 min of recording (blue circles; $n = 8$ cells). **C**, Example voltage-clamp traces after excising a nucleated patch of delayed rectifier K^+ current at baseline during activation protocol evoked from -50 -mV holding potential (5-mV increments, up to $+20$ mV; patch #180510p3). **D**, Summary plot of voltage dependence of activation of delayed rectifier K^+ current at baseline (white circles) and after 25 min of recording (blue circles; $n = 6$ cells). Dashed line depicts baseline activation curve measured in whole-cell configuration from **B**.

baseline and hyperpolarized to -46.8 ± 1.3 mV at 25 min ($t = -10.13$, $p < 0.001$; $n = 6$ cells). Likewise, the threshold shifted from -38.1 ± 0.8 mV at baseline with $CdCl_2$ to -47.7 ± 1.3 mV after 25 min of recording ($t = -7.69$, $p = 0.0015$; $n = 5$ cells). Taken together, these data demonstrate that I_A , I_K , I_h and VGCCs do not contribute to the hyperpolarization of AP threshold of SCs, consistent with our hypothesis that the primary mechanism for the shift is mediated by Na^+ channels.

Revised Hodgkin–Huxley model recapitulates the increase in SC excitability

Based on the voltage-clamp data, we revised the Hodgkin–Huxley model to match the observed changes in I_{Na} and I_A (see Materials and Methods). To do this, we targeted only their activation/inactivation properties without altering their conductances. Specifically, $v_{m_{Na}}$ was shifted

by -7 mV and $v_{h_{Na}}$ by -8.5 mV, while v_{n_A} was shifted by -14 mV and v_{h_A} by -16 mV (Table 1), which reproduced well the observed increase in excitability of SCs (Fig. 10A–D). With respect to the changes in the AP cycle described earlier (Fig. 3), the revised model captures all the cardinal features seen in the experimental recordings (Fig. 10A,B). Specifically, the AP threshold of the revised model hyperpolarized by -5.8 mV from -38.7 to -44.5 mV, which agrees well with the -6.0 -mV hyperpolarization observed experimentally. The simulated AP maximum hyperpolarized by -8.4 mV from 3.9 to -4.5 mV, which is comparable to the hyperpolarization of -8.8 mV measured experimentally. Finally, the AHP minimum observed in the revised model depolarized by $+1.8$ mV from -60.1 to -58.3 mV, which is within the margin of error of the experimental results (Fig. 3C). The fact that these specific adjustments are able to closely capture the dynamics observed exper-

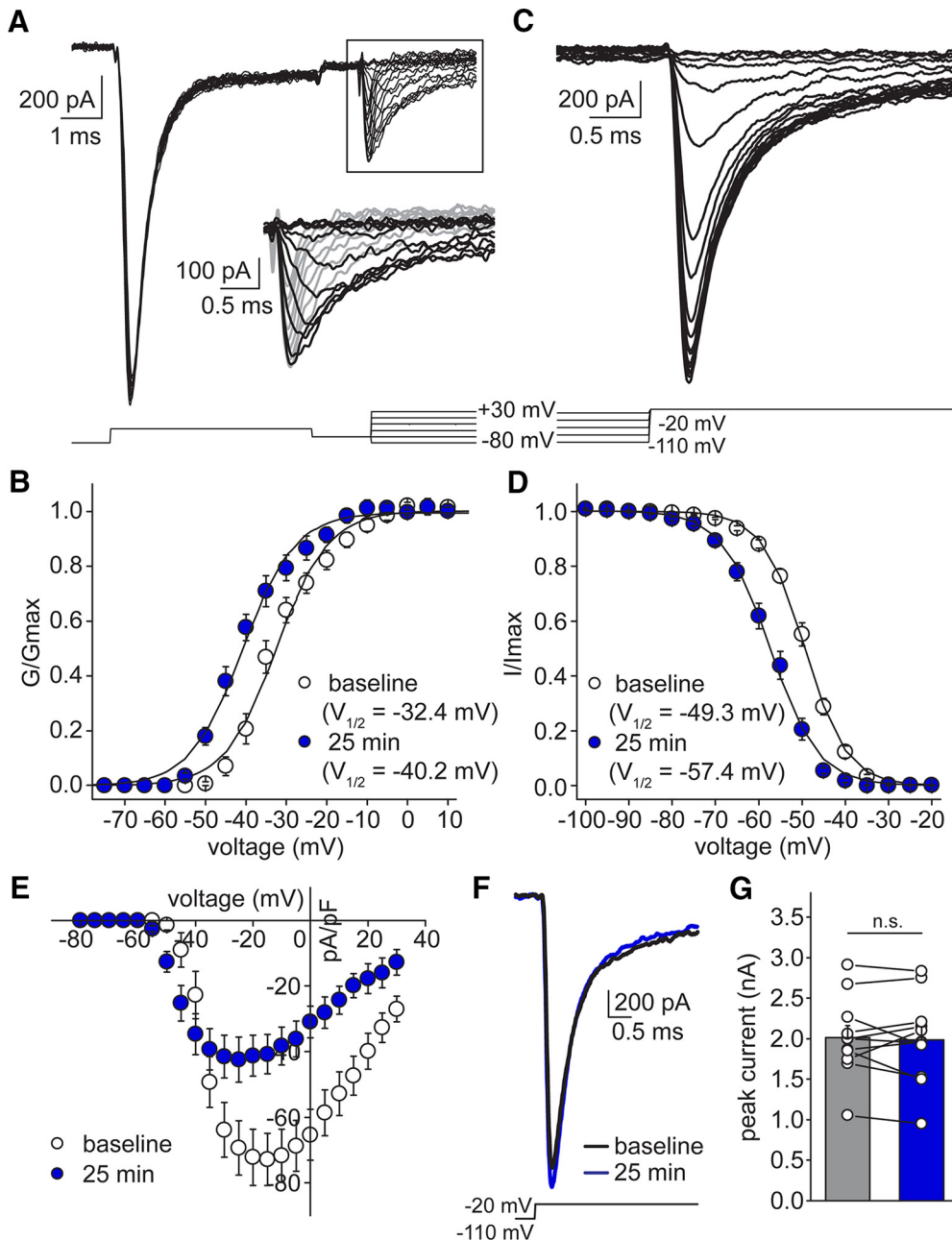


Figure 8. Na⁺ current SCs exhibits shift in both activation and inactivation properties, but not current density. **A**, Example voltage-clamp traces of Na⁺ currents evoked with a prepulse protocol (patch #170222p4). Inset, Zoom-in of portion of traces depicting strong voltage-clamp of Na⁺ currents evoked after prepulse. **B**, Summary plot of voltage dependence of activation of Na⁺ current at baseline (white circles) and at 25 min (blue circles; n = 11 cells). **C**, Example traces from a Na⁺ inactivation protocol (patch #170222p4). **D**, Summary plot of voltage dependence of inactivation at baseline (white circles) and at 25 min (blue circles; n = 11 cells). **E**, Summary current density-voltage plot (data used to construct peak conductance-voltage plots in **B**, **D**), of sodium responses at baseline (white circles) and at 25 min (blue circles). **F**, Example peak sodium current traces evoked by a -110 mV probe at baseline (black) and at 25 min (blue; patch #171108p3). **G**, Summary graph of peak sodium currents evoked from a holding potential of -110 mV at baseline (gray) and at 25 min (blue). n.s. denotes p > 0.05.

imentally further supports the dominance of I_{Na} in driving the increase in SC excitability, with an additional role for I_A in further modulating AP firing.

Discussion

The present study advances our understanding of the neurophysiology of cerebellar SCs in two important ways. First, we identify a predominant role of voltage-gated Na⁺

channels in upregulating the excitability of cerebellar SCs following membrane patch breakthrough. Under these conditions, the threshold for AP initiation is shifted to more hyperpolarized membrane potentials due to changes in the activation and inactivation properties of Na⁺ channels. Since similar shifts in gating behavior are observed in other central neurons by physiologic stimuli, such as

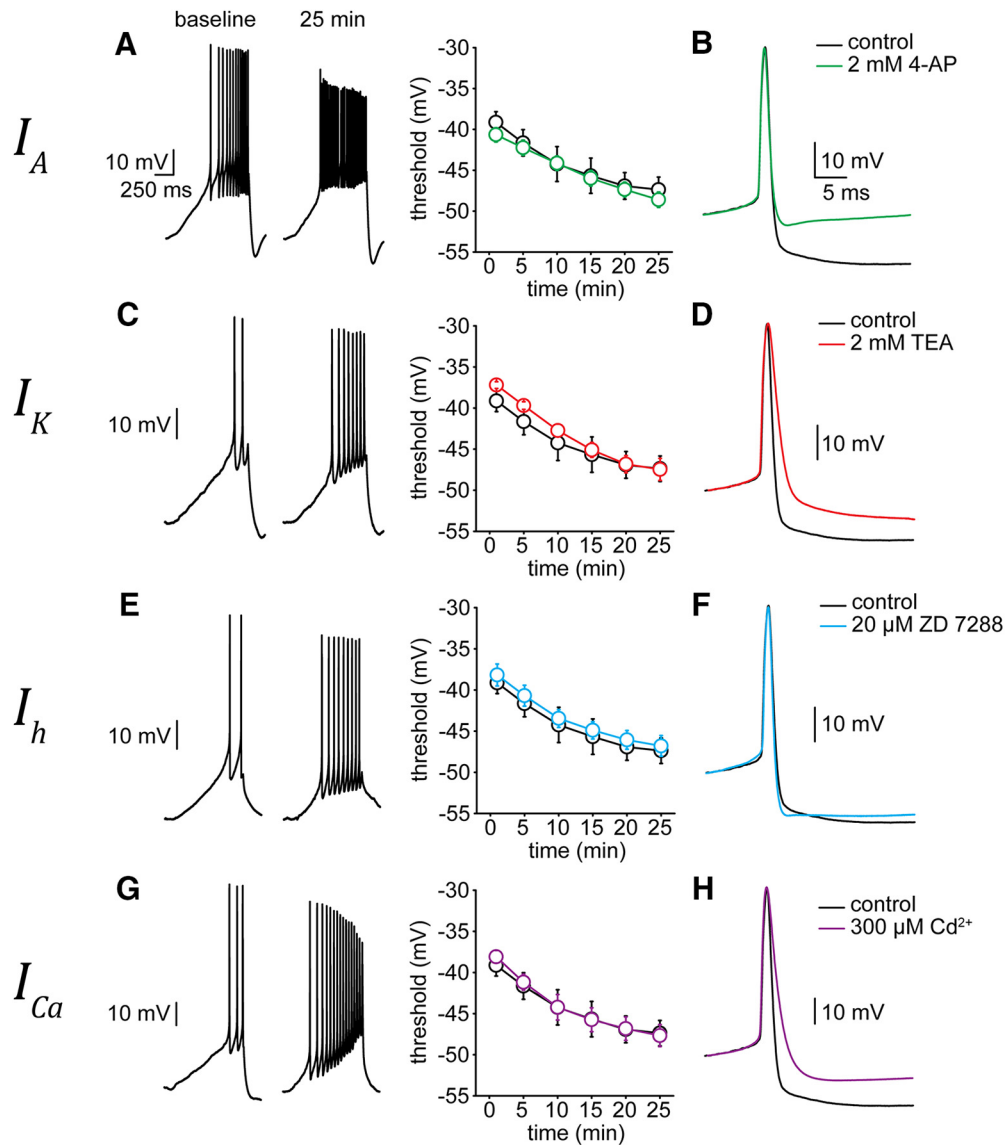


Figure 9. AP threshold hyperpolarization persists with pharmacological blockade of I_K , I_A , I_{Ca} and I_h . **A**, left panel, Example traces recorded at baseline and after 25 min of APs evoked by a current ramp protocol (25 pA over 1 s) in a SC. Right panel, Summary AP threshold data for control conditions (black open circles; $n = 6$ cells) and in the presence of 2 mM TEA in the aCSF (red open circles; $n = 5$ cells). **B**, Superimposed first APs evoked by ramp protocol in control (black) and external TEA (red) conditions. TEA scaled to control (patch #181008p8). **C**, **D**, Same as **A**, **B**, but in the presence of 2 mM 4-AP (green lines; $n = 5$ cells; patch #181015p7). **E**, **F**, Same as **A**, **B**, but in the presence of 20 μ M ZD 7288 (blue lines; $n = 6$ cells; patch #181018p2). **G**, **H**, Same as **A**, **B**, but in the presence of 200–300 μ M CdCl₂ (purple lines; $n = 5$ cells; patch #181024p4).

NMDA receptor activation (Xu et al., 2005), it is possible that Na⁺ channels are targeted in a comparable manner in SCs to upregulate AP firing. Second, we report hyperpolarizing shifts in both the activation and inactivation properties of A-type K⁺ channels that contribute to the time-dependent increase in firing rates observed in SCs but do not participate in the hyperpolarizing shift in AP threshold. Previous work has established that depolarizing shifts in A-type K⁺ channel inactivation are triggered by elevations in cytosolic Ca²⁺ due to T-type Ca²⁺ channel activity in SCs (Molineux et al., 2005; Anderson et al., 2010, 2013). Given this distinction with the present study, it is likely that different signaling events are at

play to regulate the gating behavior of A-type K⁺ channels in cerebellar SCs.

Increased membrane excitability following whole-cell recording is not unique to SCs

SCs are not the only neuronal cell type that undergo functional changes after the establishment of the whole-cell patch-clamp configuration. In fact, early patch clamp studies of voltage-gated ion channels noted time-dependent changes in both activation and inactivation properties including changes to voltage-gated Na⁺ channels (Fenwick et al., 1982; Fernandez et al., 1984; Vandenberg and Horn, 1984; Marty and Neher, 1985). The

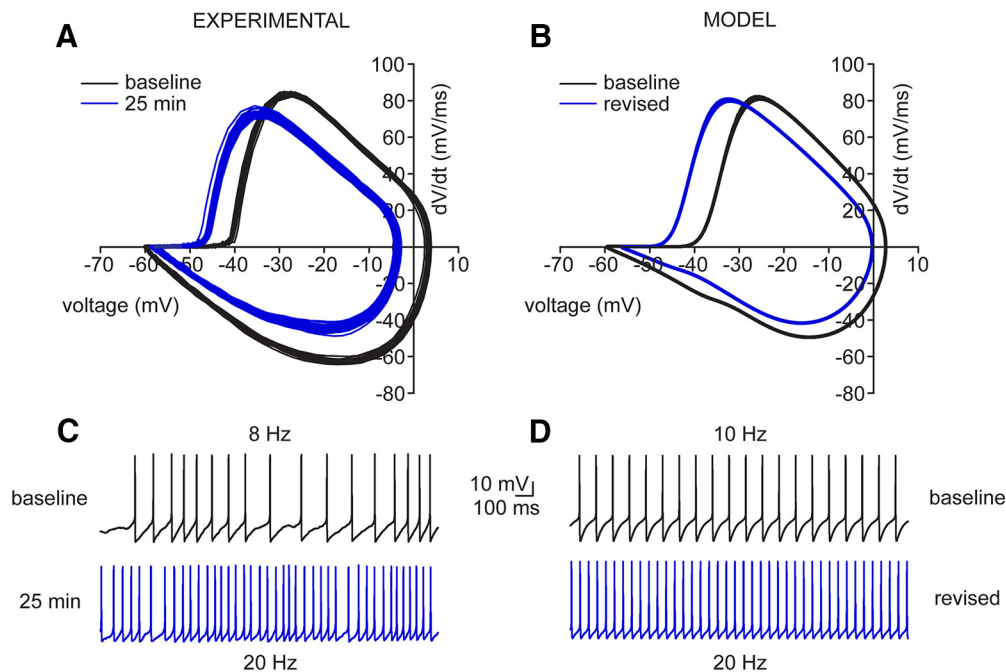


Figure 10. Voltage-clamp-informed model recapitulates the dynamics of current-clamp experimental data. **A**, AP cycle calculated from experimental SC current-clamp recording at baseline (black) and 25 min (blue). **C**, Same current-clamp recording data as above, presented as voltage versus time at baseline (black) and 25 min (blue). **B**, Simulated AP cycle of baseline (black) and revised (blue) models after modifying all gating parameters based on values measured experimentally in voltage-clamp in SCs. **D**, Simulated firing properties of baseline (black) and revised (blue) models.

mechanism(s) underlying these changes has remained largely unexplored and thus ignored - as has been the case for cerebellar SCs. In the cerebellum, the increased firing rate we have observed in GCs (compare Fig. 1) may be attributed to the cell's buffering capacity for cytosolic Ca^{2+} which is further compromised when GCs lack the calcium binding protein, calretinin (Gall et al., 2003). Similarly, Alcami and colleagues also linked a rise in intracellular Ca^{2+} to an increase in firing rates of SCs (Alcami et al., 2012) suggesting that there may be overlapping signaling pathways at play in both cell types (see below). A distinction with SCs, however, is that we have observed an increase in the input resistance of GCs following patch breakthrough. Whether the change in membrane leak is due to the activity of other ion channels, such as TASK-1 (Millar et al., 2000) or HCN channels (Zúñiga et al., 2016), in GCs remains to be studied. Why the excitability of SCs and GCs increases after patch breakthrough whereas Purkinje cells remain stable is not clear. It is tempting to speculate that the smaller soma of SCs makes their subcellular Ca^{2+} stores more susceptible to perturbation during whole-cell recording compared to Purkinje cells. It is also possible that SCs are mechanosensitive which is in keeping with the observation that SC excitability increases during cell-attached recordings, particularly in recordings with a tight seal (Alcami et al., 2012). As discussed below, the events that are initiated by membrane patch breakthrough suggest that voltage-gated Na^+ channels may be impacted by several endogenous signaling pathways in SCs.

Expression and regulation of Na^+ channels in cerebellar SCs

Cerebellar MLIs are thought to express several Na^+ channel pore-forming subunits that include Nav1.1, Nav1.2, and Nav1.6 (Schaller and Caldwell, 2003); however, more recent data suggest that the Nav1.2 protein is expressed only on presynaptic terminals of GCs (Jarnot and Corbett, 2006; Martínez-Hernández et al., 2013). This latter finding agrees with our experiments using the Nav1.2-selective inhibitor, Phrixotoxin-III, which has negligible pharmacological effect on SC excitability (Alexander and Bowie, unpublished observation). Based on antibody staining, both Nav1.1 and Nav1.6 subunits are expressed in MLIs (Kalume et al., 2007); however, their subcellular distribution is distinct (Lorincz and Nusser, 2008). The Nav1.6 subunit is almost exclusively expressed at the axon initial segment (AIS), a region of the axon close to the cell body where APs are initiated. In contrast, Nav1.1 is expressed throughout the axon, although it is also found in the proximal AIS (Lorincz and Nusser, 2008). Given this arrangement, both Nav1.1 and Nav1.6 subunits may contribute to the Na^+ channel currents we have recorded from SCs. Whether these subunits are also expressed in the dendrites has not been formally investigated, although SC dendrites are apparently devoid of Na^+ channels (Myoga et al., 2009). It is curious that the expression pattern of the delayed rectifier K^+ channel subunits, Kv1.1 and Kv1.2, overlap with Nav1.6 subunits, but yet, are not subject to modulation following patch breakthrough (compare Fig. 9). This observation suggests that the signaling pathway(s) that promotes gating shifts in Na^+

channels is tightly compartmentalized from other ion channels, such as Kv1.1 and Kv1.2, even within the AIS.

Gating shifts in Na⁺ channel activation and inactivation, as observed in the present study (compare Fig. 8), may, in principle, be mediated by a number of mechanisms that include direct binding by cytosolic Ca²⁺, binding of the Ca²⁺-calmodulin complex and/or changes in the phosphorylation state of the Na⁺ channel (Cantrell and Catterall, 2001; Van Petegem et al., 2012). Regulation of recombinant Nav1.6 channels has primarily focused on the effect of channel phosphorylation where protein kinase A (PKA) stimulation (Chen et al., 2008) and p38 mitogen-activated protein kinase (Wittmack et al., 2005) both cause a reduction in peak Na⁺ channel current. In the latter case, the reduction in current density did not affect channel gating (Wittmack et al., 2005), unlike the present study (compare Fig. 8) but was due to the internalization of Nav1.6 channels (Gasser et al., 2010). In contrast, inhibition of glycogen-synthase kinase 3 β (GSK3 β) causes a decrease in recombinant Nav1.6 responses (Scala et al., 2018) suggesting that phosphorylation sustains channel activity in HEK 293 cells. Likewise, in medium spiny neurons of the nucleus accumbens, regulation of GSK3 β activity impacts firing rates in a Nav1.6-dependent manner (Scala et al., 2018) suggesting that phosphorylation and dephosphorylation events may be critical in fine-tuning neuronal output. Much less is known about the regulation of Nav1.1 channels, although, earlier recombinant studies and more recent proteomic work has identified putative phosphorylation sites which often overlap with sites identified for Nav1.2 channels (Smith and Goldin, 1998; Berendt et al., 2010). Interestingly, forskolin activation of PKA causes a hyperpolarizing shift in both the activation and inactivation curves for recombinant Nav1.1 (Liu and Zheng, 2013) as observed in the present study on cerebellar SCs. An identical gating shift is observed in hippocampal CA1 pyramidal cells, probably mediated by Nav1.2 channels, that is triggered by NMDA receptor activation and the activity of CaM kinase II (Xu et al., 2005). Given the similarity in how Nav1.1 and Nav1.2 channels are regulated by phosphorylation, it would be interesting to test if a NMDA receptor-mediated signaling pathway could induce a similar shift in the gating behavior of Na⁺ channels in cerebellar SCs. Likewise, experiments using dynamic clamp to test the effect of a Nav channel gating model on SC excitability would be interesting to test in future studies.

Multiple families of voltage-gated ion channels control SC excitability

Although SCs express a variety of voltage-gated ion channels, somatodendritic A-type K⁺ channels are an important regulator of their firing rates (Molineux et al., 2005; Anderson et al., 2010, 2013). Specifically, AP firing rates are regulated by Kv4.2/4.3 subunits whose basal activity is fine-tuned by elevations in cytosolic Ca²⁺ mediated by the Ca²⁺ channel subunits, Cav3.2 and Cav3.3 (Anderson et al., 2010). Both ion channel families form a signaling complex through the modulatory protein, KChIP3, which contains an E-F hand and thus is able to

act as a Ca²⁺ sensor that couples the activity of Ca²⁺ channels to the regulation of K⁺ channels (Pongs and Schwarz, 2010). Elevations in intracellular Ca²⁺ selectively promote depolarizing shifts in steady-state inactivation of A-type K⁺ channels and, in doing so, attenuate membrane depolarization and AP firing (Anderson et al., 2010, 2013). In contrast, our data establish that A-type K⁺ channels contribute to an increase in AP firing of SCs via a hyperpolarizing shift in channel activation and inactivation (compare Fig. 6). Although the formation of the whole-cell recording is likely to elevate cytosolic Ca²⁺ in SCs, as discussed above, the shifts A-type K⁺ channel gating observed in this study are probably not reliant on KChIP3 modulation. Finally, although other voltage-gated ion channels may be involved in controlling SC excitability, pharmacological block of many of these channels (Fig. 9) reveals that they do not impact AP threshold. Consequently, our work identifies a predominant role of voltage-gated Na⁺ channels in upregulating the firing rates of cerebellar SCs.

References

- Alcami P, Franconville R, Llano I, Marty A (2012) Measuring the firing rate of high-resistance neurons with cell-attached recording. *J Neurosci* 32:3118–3130.
- Anderson D, Mehaffey WH, Iftinca M, Rehak R, Engbers JD, Hameed S, Zamponi GW, Turner RW (2010) Regulation of neuronal activity by Cav3-Kv4 channel signaling complexes. *Nat Neurosci* 13:333–337.
- Anderson D, Engbers JD, Heath NC, Bartoletti TM, Mehaffey WH, Zamponi GW, Turner RW (2013) The Cav3-Kv4 complex acts as a calcium sensor to maintain inhibitory charge transfer during extracellular calcium fluctuations. *J Neurosci* 33:7811–7824.
- Armstrong DM, Rawson JA (1979) Activity patterns of cerebellar cortical neurones and climbing fibre afferents in the awake cat. *J Physiol* 289:425–448.
- Astorga G, Li D, Therreau L, Kassa M, Marty A, Llano I (2017) Concerted interneuron activity in the cerebellar molecular layer during rhythmic oromotor behaviors. *J Neurosci* 37:11455–11468.
- Berendt FJ, Park KS, Trimmer JS (2010) Multisite phosphorylation of voltage-gated sodium channel alpha subunits from rat brain. *J Proteome Res* 9:1976–1984.
- Bers DM, Patton CW, Nuccitelli R (2010) A practical guide to the preparation of Ca(2+) buffers. *Methods Cell Biol* 99:1–26.
- Cantrell AR, Catterall WA (2001) Neuromodulation of Na⁺ channels: an unexpected form of cellular plasticity. *Nat Rev Neurosci* 2:397–407.
- Carter AG, Regehr WG (2002) Quantal events shape cerebellar interneuron firing. *Nat Neurosci* 5:1309–1318.
- Chen Y, Yu FH, Sharp EM, Beacham D, Scheuer T, Catterall WA (2008) Functional properties and differential neuromodulation of Nav1.6 channels. *Mol Cell Neurosci* 38:607–615.
- Christie JM, Jahr CE (2008) Dendritic NMDA receptors activate axonal calcium channels. *Neuron* 60:298–307.
- Dani JA, Sanchez JA, Hille B (1983) Lyotropic anions. Na channel gating and Ca electrode response. *J Gen Physiol* 81:255–281.
- Duguid IC, Smart TG (2004) Retrograde activation of presynaptic NMDA receptors enhances GABA release at cerebellar interneuron-Purkinje cell synapses. *Nat Neurosci* 7:525–533.
- Fenwick EM, Marty A, Neher E (1982) Sodium and calcium channels in bovine chromaffin cells. *J Physiol* 331:599–635.
- Fernandez JM, Fox AP, Krasne S (1984) Membrane patches and whole-cell membranes: a comparison of electrical properties in rat clonal pituitary (GH3) cells. *J Physiol* 356:565–585.

- Gaffield MA, Christie JM (2017) Movement rate is encoded and influenced by widespread, coherent activity of cerebellar molecular layer interneurons. *J Neurosci* 37:4751–4765.
- Gall D, Roussel C, Susa I, D'Angelo E, Rossi P, Bearzatto B, Galas MC, Blum D, Schurmans S, Schiffmann SN (2003) Altered neuronal excitability in cerebellar granule cells of mice lacking calretinin. *J Neurosci* 23:9320–9327.
- Gasser A, Cheng X, Gilmore ES, Tyrrell L, Waxman SG, Dib-Hajj SD (2010) Two Nedd4-binding motifs underlie modulation of sodium channel Nav1.6 by p38 MAPK. *J Biol Chem* 285:26149–26161.
- Glitsch M, Marty A (1999) Presynaptic effects of NMDA in cerebellar Purkinje cells and interneurons. *J Neurosci* 19:511–519.
- Häusser M, Clark BA (1997) Tonic synaptic inhibition modulates neuronal output pattern and spatiotemporal synaptic integration. *Neuron* 19:665–678.
- Jarnot M, Corbett AM (2006) Immunolocalization of Nav1.2 channel subtypes in rat and cat brain and spinal cord with high affinity antibodies. *Brain Res* 1107:1–12.
- Jörntell H, Ekerot CF (2003) Receptive field plasticity profoundly alters the cutaneous parallel fiber synaptic input to cerebellar interneurons in vivo. *J Neurosci* 23:9620–9631.
- Kaczorowski CC, Disterhoft J, Spruston N (2007) Stability and plasticity of intrinsic membrane properties in hippocampal CA1 pyramidal neurons: effects of internal anions. *J Physiol* 578:799–818.
- Kalume F, Yu FH, Westenbroek RE, Scheuer T, Catterall WA (2007) Reduced sodium current in Purkinje neurons from Nav1.1 mutant mice: implications for ataxia in severe myoclonic epilepsy in infancy. *J Neurosci* 27:11065–11074.
- Liu H, Zhao SN, Zhao GY, Sun L, Chu CP, Qiu DL (2014) N-methyl-D-aspartate inhibits cerebellar Purkinje cell activity via the excitation of molecular layer interneurons under in vivo conditions in mice. *Brain Res* 1560:1–9.
- Liu S, Zheng P (2013) Altered PKA modulation in the Nav1.1 epilepsy variant I1656M. *J Neurophysiol* 110:2090–2098.
- Liu SJ, Lachamp P (2006) The activation of excitatory glutamate receptors evokes a long-lasting increase in the release of GABA from cerebellar stellate cells. *J Neurosci* 26:9332–9339.
- Lorincz A, Nusser Z (2008) Cell-type-dependent molecular composition of the axon initial segment. *J Neurosci* 28:14329–14340.
- Martínez-Hernández J, Ballesteros-Merino C, Fernández-Alacid L, Nicolau JC, Aguado C, Luján R (2013) Polarised localisation of the voltage-gated sodium channel Nav1.2 in cerebellar granule cells. *Cerebellum* 12:16–26.
- Marty A, Neher E (1985) Potassium channels in cultured bovine adrenal chromaffin cells. *J Physiol* 367:117–141.
- Midtgaard J (1992) Membrane properties and synaptic responses of Golgi cells and stellate cells in the turtle cerebellum in vitro. *J Physiol* 457:329–354.
- Milescu LS, Bean BP, Smith JC (2010) Isolation of somatic Na⁺ currents by selective inactivation of axonal channels with a voltage prepulse. *J Neurosci* 30:7740–7748.
- Millar JA, Barratt L, Southan AP, Page KM, Fyffe RE, Robertson B, Mathie A (2000) A functional role for the two-pore domain potassium channel TASK-1 in cerebellar granule neurons. *Proc Natl Acad Sci USA* 97:3614–3618.
- Molineux ML, Fernandez FR, Mehaffey WH, Turner RW (2005) A-type and T-type currents interact to produce a novel spike latency-voltage relationship in cerebellar stellate cells. *J Neurosci* 25:10863–10873.
- Myoga MH, Beierlein M, Regehr WG (2009) Somatic spikes regulate dendritic signaling in small neurons in the absence of backpropagating action potentials. *J Neurosci* 29:7803–7814.
- Pongs O, Schwarz JR (2010) Ancillary subunits associated with voltage-dependent K⁺ channels. *Physiol Rev* 90:755–796.
- Saitow F, Konishi S (2000) Excitability increase induced by beta-adrenergic receptor-mediated activation of hyperpolarization-activated cation channels in rat cerebellar basket cells. *J Neurophysiol* 84:2026–2034.
- Scala F, Nenov MN, Crofton EJ, Singh AK, Folorunso O, Zhang Y, Chesson BC, Wildburger NC, James TF, Alshammari MA, Alshammari TK, Elfrink H, Grassi C, Kasper JM, Smith AE, Hommel JD, Lichti CF, Rudra JS, D'Ascenzo M, Green TA, et al. (2018) Environmental enrichment and social isolation mediate neuroplasticity of medium spiny neurons through the GSK3 pathway. *Cell Rep* 23:555–567.
- Schaller KL, Caldwell JH (2003) Expression and distribution of voltage-gated sodium channels in the cerebellum. *Cerebellum* 2:2–9.
- Smith RD, Goldin AL (1998) Functional analysis of the rat I sodium channel in xenopus oocytes. *J Neurosci* 18:811–820.
- Townsend C, Hartmann HA, Horn R (1997) Anomalous effect of permeant ion concentration on peak open probability of cardiac Na⁺ channels. *J Gen Physiol* 110:11–21.
- Van Petegem F, Lobo PA, Ahern CA (2012) Seeing the forest through the trees: towards a unified view on physiological calcium regulation of voltage-gated sodium channels. *Biophys J* 103:2243–2251.
- Vandenberg CA, Horn R (1984) Inactivation viewed through single sodium channels. *J Gen Physiol* 84:535–564.
- Wittmack EK, Rush AM, Hudmon A, Waxman SG, Dib-Hajj SD (2005) Voltage-gated sodium channel Nav1.6 is modulated by p38 mitogen-activated protein kinase. *J Neurosci* 25:6621–6630.
- Xu J, Kang N, Jiang L, Nedergaard M, Kang J (2005) Activity-dependent long-term potentiation of intrinsic excitability in hippocampal CA1 pyramidal neurons. *J Neurosci* 25:1750–1760.
- Zúñiga R, González D, Valenzuela C, Brown N, Zúñiga L (2016) Expression and cellular localization of HCN channels in rat cerebellar granule neurons. *Biochem Biophys Res Commun* 478:1429–1435.